

Amylose derived macro-porous core and micro-porous shell carbon spheres as sulfur host for superior lithium-sulfur battery cathodes

Xiang Li^a, Mingxia Gao^{a*}, Xuanbing Cheng^a, Yongfeng Liu^a, Zhengxiao Guo^b, Congxiao Shang^c, Hongge

Pan^{a*}

Abstract

Porous carbon can be tailored to great effect for electrochemical energy storage. In this study, we propose a novel structured spherical carbon with a macroporous core and a microporous shell derived from a sustainable biomass, amylose, by a multi-step pyrolysis route without chemical etching. This hierarchically porous carbon shows a particle distribution of 2–10 μm and a surface area of 672 $\text{m}^2 \text{g}^{-1}$. The structure is an effective sulfur host for lithium-sulfur battery cathodes, reduces the dissolution of polysulfides in the electrolyte and offers high electrical conductivity during discharge/charge cycling. The hierarchically porous carbon can hold 48 wt% sulfur mostly in its porous structure. The S@C hybrid shows an initial capacity of 1490 mA h g^{-1} and retains a capacity of 798 mA h g^{-1} after 200 cycles at a discharge/charge rate of 0.1 C. A capacity of 487 mA h g^{-1} is obtained at 3 C rate. A one-step pyrolysis and a chemical reagent assisted pyrolysis are also assessed to obtain

^a State Key Laboratory of Silicon Materials, Key Laboratory of Advanced Materials and Applications for Batteries of Zhejiang Province & School of Materials Science and Engineering, Zhejiang University, Hangzhou 310027, P.R. China. E-mail addresses: gaomx@zju.edu.cn (M Gao); hapan@zju.edu.cn (H Pan), Tel./Fax: +86 571 87952615.

^b Department of Chemistry, University College London, London, WC1H 0AJ, UK

^c School of Environmental Sciences, University of East Anglia, Norwich, NR4 7TJ, UK

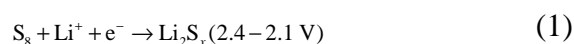
†Electronic supplementary information (ESI) available: TG/MS curves of amylose; XRD patterns of the differently carbonized amylose and the S@C hybrids; EDS analysis of the S@C hybrids; TG curves of the sulfur impregnated S@C systems; Differential capacity to potential (dQ/dV) profiles of the S@C hybrids at the first and 200th cycles at 0.1 C, and at the initial cycle at different rates.

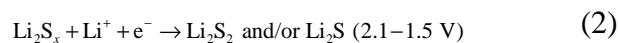
porous carbon from amylose, but the obtained carbon shows inferior structures for sulfur cathodes. The multi-step pyrolysis and the resulting hierarchically porous carbon offer an effective approach to the engineering of biomass for energy storage. The micron-sized spherical S@C hybrid with different sizes is also favorable for high-tap density and hence the volumetric density of the batteries, opening up a wide scope for practical applications.

Introduction

Under the dual pressure of emission reduction and economic development, developing naturally sustainable, abundant and low-cost materials for energy storage materials is highly desirable. Carbonaceous materials originated from biomass have received considerable attention in the application of energy storage devices with the increasing consciousness of sustainability and environmental benignity.¹ Versatile biomass carbon sources in nature offer wide choices in producing carbon of different structures that are required in energy storage, such as the carbonized bean shell used for electric double layer capacitors and lithium-ion battery anodes,² peanut shell derived hard carbon as anode materials for lithium and sodium batteries,³ cotton,⁴ apricot shell,⁵ silk cocoon⁶ and shaddock peel⁷ as sulfur hosts for lithium-sulfur battery cathodes after carbonization.

Lithium-sulfur batteries (LSBs) have attracted substantial interest in recent years due to their high-energy density.⁸ The electrochemical reactions between lithium metal and sublimed sulfur can be expressed by the following reactions:⁹





The theoretical capacity of sulfur cathode is 1672 mA h g⁻¹, assuming that a complete reaction product of Li₂S is formed¹⁰. However, the long-chain lithium polysulfides (2 < x ≤ 8) generated in reaction (1) is soluble in the electrolyte of the LSBs, subsequently causing shuttling effect with the short-chain Li₂S₂/Li₂S between cathode and anode during charging, which decreases the utilization of the overall active material during cycling. Moreover, sulfur and Li₂S_x (x = 1–8) have poor ionic and electronic conductivities, hence the internal resistance of the batteries is large and the reaction kinetics is sluggish. The early formed insoluble insulated layer of Li₂S/Li₂S₂ on the surface of the sulfur particles during discharge impedes the continuous reduction of S, which leads to poor active material utilization.¹¹ The volume variation of sulfur during cycling is another problem. The volume expansion from S₈ (with a density of 2.07 g cm⁻³) to Li₂S (with a density of 1.66 g cm⁻³)¹² is *ca.* 79%, which causes pulverization of Li₂S, and thus damages the electrical contacts between the Li₂S particles and hence the integrity of the electrode. Therefore, challenges exist in achieving high cyclic stability and rate capability for LSBs.

To overcome the aforementioned problems of dissolution, low conductivity and volume expansion of the cathode material in LSBs, an effective and widely used method is to incorporate sulfur into porous conductive carbon matrix, such as mesoporous carbon hollow spheres,^{13, 14} microporous carbon spheres,¹⁵ hierarchical porous graphene sheets.¹⁶

Alternatively, infiltrating sulfur into the tubes of carbon nanotubes,¹⁷ impregnating sulfur in porous microsphere frameworks composed of multi-wall carbon nanotubes,¹⁸ wrapping sulfur by graphene,^{19, 20} or coating conductive polymers on the surface of sulfur particles.^{21, 22} The above approaches sequester relatively the direct contact of sulfur and its lithiation products of polysulfides with the electrolyte, and hence reduce the dissolution of polysulfides in the electrolyte. The porous carbon host and the conductive polymer coatings also improve the electron conductivity of the sulfur cathode and accommodate the volume change of sulfur during cycling. As a result, the electrochemical properties of sulfur cathodes are improved. In addition, other method, such as electrodepositing sulfur nanodots on Ni foam coupling with adding Li_2S_8 as additive in the electrolyte²³ and in situ synthesis of nano sulfur particles distributed three-dimensional porous graphitic carbon composites²⁴ also show significance in achieving high performance sulfur cathodes.

Compared with engineering carbonaceous materials, biomass derived carbonaceous materials are abundant, renewable and environmentally friendly. Such materials have been considered as carbon hosts for sulfur cathodes for LSBs in recent years, including those from Apricot shell,⁵ silk cocoon,⁶ shaddock peel,⁷ bamboo charcoal,²⁵ cotton²⁶ and pig bone,²⁷ etc. KOH assisted pyrolysis is the commonly used method for carbonization.^{6, 7, 27} Hierarchically porous and microporous structures with surface areas of $900\text{--}3200\text{ m}^2\text{ g}^{-1}$ are achievable.^{6, 7, 27} After incorporating sulfur contents of 50–68 wt%, those S@C

hybrids^{6, 7, 27} show favorable capacities and capacity retention. In addition, besides the application as porous carbon hosts for sulfur cathodes, biomass derived carbonaceous materials are also reported for other applications in LSBs. For instance, a filamentous fungi derived carbon-fiber monolith²⁸ and bamboo carbon fiber membrane²⁹ are used as a conductive porous captor interlayer for lithium polysulfides between sulfur cathode and separator. A carbonized eggshell membrane is also used as a natural polysulfide reservoir for LIBs.³⁰ Those are all effective in improving electrochemical properties. However, the electrochemical properties of the biomass derived S@C hybrids still need to be further improved in order to realize their practical applications. Exploring new biomass carbon sources and structures are important in order to develop high-performance S@C hybrids.

Amylose is an abundant biopolymer in nature, with a chemical formula, $C_{12}H_{22}O_{11}$. In this work, different pyrolysis methods, including multi-step pyrolysis, one-step pyrolysis and KOH (potassium hydroxide) etching assisted pyrolysis, were used to carbonize amylose in order to obtain optimized porous carbons as sulfur hosts for superior LSB cathodes. A micron-sized spherical hierarchical porous carbon with macroporous core and microporous shell was obtained by the multi-step pyrolysis (the obtained carbon is abbreviated as MHPC) without oxide templates, which is commonly used in the synthesis of porous spherical carbon.^{7, 14} The carbon shows a high surface area and high porosity. The hierarchical porous structure can accommodate 46 wt.% S (S_8)

compactly in the pores. The obtained S@MHPC hybrid shows superior electrochemical properties for LSB cathodes. While the one-step pyrolytic carbon (abbreviated as OSPC) and the KOH etching assisted pyrolytic carbon (abbreviated as KEAC) show lower surface area and lower porosity, exhibiting inferior electrochemical properties after incorporation with sulfur as LSB cathodes, compared with the MHPC. The present multi-step pyrolyzed spherical hierarchical porous carbon should be of great benefit to the development of carbonaceous materials from biomass for LSB cathodes. The micron-sized spherical shape also facilitates high packing density for the cathodes, favoring the volumetric capacity of the batteries, which is important for practical applications.

Experimental

Material preparation

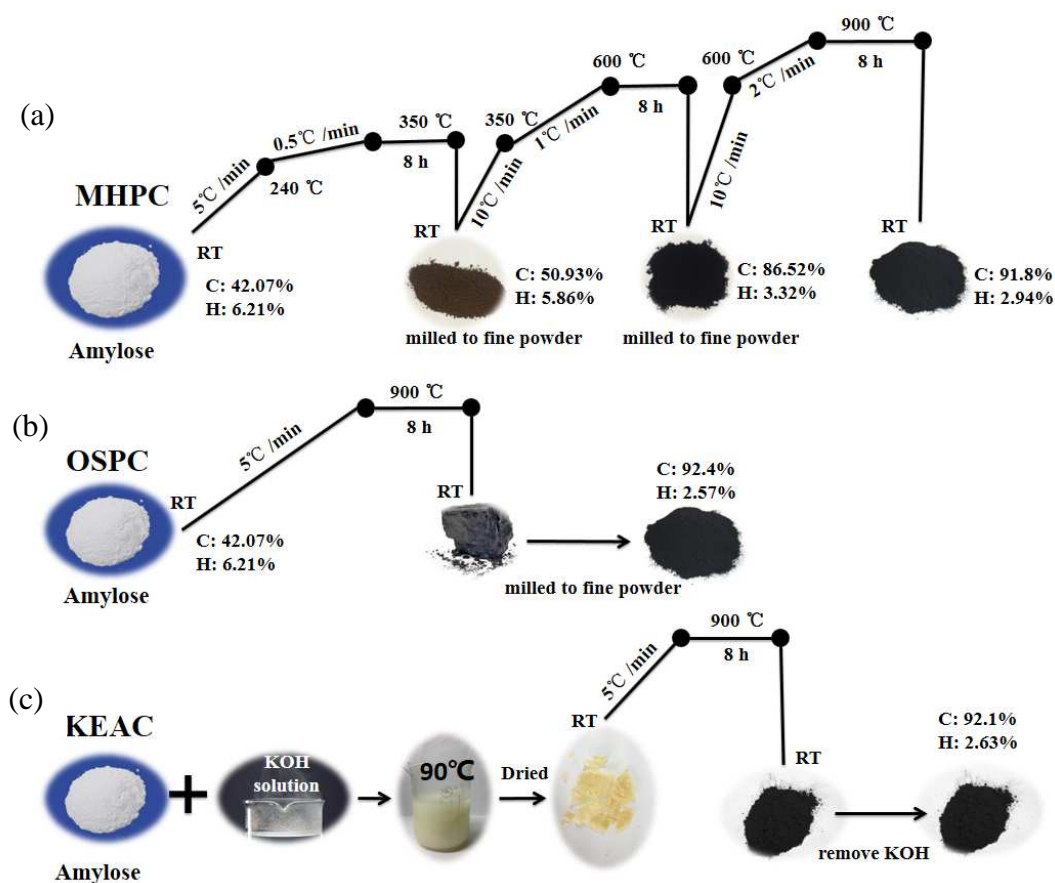
From the TG (thermal gravimetric) and MS (mass spectrum) measurements (Hiden Analytical QIC-20) of the amylose (Supporting information, Fig. S1), it is known that the main weight loss initiates at 260 °C and completes at 360 °C, showing a value of 57%, which is from the loss of H₂O. Negligible amounts of CO₂ and CO were released at the temperature range of 270–320 °C. The weight loss from 360 up to 650 °C is only of *ca.* 7 wt.%, including the release of H₂ over 450 °C.

Give that amylose has a high concentration of water, controlling the generation rate of steam during carbonization is important to avoid the collapse

of the original morphology of amylose. In this case, a multi-step pyrolysis method was proposed to carbonize amylose, as shown in Scheme 1a. Amylose was firstly heated to 240 °C at a heating rate of 5 °C min⁻¹ and then to 350 °C at a rate of 0.5 °C min⁻¹, where it was held for 8 h in flowing Ar at a rate of 2 L min⁻¹. After cooling, the initially heat-treated amylose was milled to fine powder in an agate mortar, and then heated to 350 °C at a rate of 10 °C min⁻¹ and to 600 °C at a rate of 1 °C min⁻¹, where it was held for 8 h in flowing Ar with a rate of 1 L min⁻¹. The obtained powder was grounded in an agate mortar again, and then heated to 600 °C at a rate of 10 °C min⁻¹ and to 900 °C at a rate of 2 °C min⁻¹, maintaining for 8 h in flowing Ar with a flow rate of 1 L min⁻¹. After cooling, the finally obtained powder (MHPC) was used for structural characterization and for sulfur host without further milling. For comparison, one-step pyrolysis of amylose by heating to 900 °C at a rate of 5 °C min⁻¹ and maintaining for 8 h in flowing Ar with a rate of 2 L min⁻¹, as shown in Scheme 1b, is also performed. The obtained powder (OSPC) was milled by agate mortar prior to structural characterization and for sulfur host.

In addition, in order to obtain other desirable carbon structures, a chemical etching assisted pyrolysis method, as shown in Scheme 1c, was also used. Typically, 5 g of amylose is mixed with 100 ml 1 mol L⁻¹ KOH aqueous solution by stirring at 90 °C. (what's the purpose / underline-principles of etching before carbonization?) After the water was completely evaporated, the mixture was heated to 900 °C at a rate of 2 °C min⁻¹ and maintained for 8 h

in flowing Ar with a rate of 2 L min^{-1} . After cooling, the product was rinsed by stirring with 250 ml of 0.5 M HCl solution, which was further leached by distilled water at room temperature for several times, until the pH value of the filtrate was 7. The leached product was then dried in vacuum at $160 \text{ }^\circ\text{C}$ for 24 h. The obtained product (KEAC) was used for structural characterization and for sulfur host without further milling. Graphite crucible was used as the container for the pyrolysis of all the samples.



Scheme 1 Schematic routes of the preparation process for MHPC (a), OSPC (b) and KEAC (c).

(How the C,H contents determined? How about O content, which may influence the conductivity of the carbon).

For preparation of S@C hybrids, the obtained carbon powder was firstly

mixed with sulfur by ball milling in a weight ratio of 1: 2, and then diverted into an airtight stainless steel container in vacuum. The container sealed with the mixture was heated at 160 °C for 24 h to infiltrate sulfur into the porous carbon to form S@C hybrids. In order to remove the sulfur covered on the surface of the carbon particles or congregated between the carbon particles, which is considered to be more easily dissolved in electrolyte and result in poor cyclic stability, the S@C hybrids were further heated at 300 °C for 0.5 h in a tube furnace under flowing Ar.

Structural analyses

Morphologies of the samples were observed by scanning electron microscopy (SEM, Hitachi S-4800). TG measurement of the S@C hybrids was performed from room temperature (RT) to 600 °C at a heating rate of 5 °C min⁻¹. A pure Ar (99.999%) was used as carrying gas. The distribution of sulfur in the S@C hybrids was detected by an energy-dispersive spectrometer (EDS, Horiba) attached to the SEM. In order to observe the inner structure of the carbonized products and the S@C hybrids, the samples were put into liquid nitrogen and kept for 5 minutes and then mechanically pressed by a pressure of 20 MPa. Pore structure of the samples was analyzed by a nitrogen sorption method (Quantachrome Nova 1000e analyzer). A temperature of 77 K was used for the measurement. Specific surface area of the samples was measured by the Brunauer-Emmet-Teller (BET) method. Pore size distribution was calculated from the adsorption branch of N₂ isotherm by the density functional theory

(DFT). Crystal structure of the samples was identified by X-ray diffraction (XRD, X'Pert PRO, PANalytical) using Cu- K_{α} radiation ($\lambda=1.5418 \text{ \AA}$) with a scanning step of $0.04^{\circ} \text{ s}^{-1}$. Raman spectra of the samples were recorded by a confocal Raman microscope (Via-Reflex) using laser beam with a wavelength of 532 nm. As sulfur is very easy to evaporate during Raman spectrum test under strong laser excitation, the laser power was kept at less than $2.5 \text{ mW } \mu\text{m}^{-2}$ and a short irradiation period of 30 s was used.

Electrochemical tests

Electrochemical properties of the S@C hybrids were measured using coin cells of CR2025 with Li foil (99.9% Alfa Aesar) as the reference and counter electrode, and a polyethylene membrane (Celgard 2400) as a separator. The working electrode was prepared by mixing the S@C hybrid, Ketjen black, carbon black and polyvinylidene difluoride (PVDF, Alfa Aesar) at a weight ratio of 75: 4: 11: 10 in 1-methyl-2-pyrrolidinone (NMP, Aldrich) to form a slurry, which was subsequently pasted onto an aluminum foil and then dried at 60°C for 24 h in vacuum. The S@C hybrid loaded on each electrode was *ca.* 1.1 mg cm^{-2} . The electrolyte consists of 1 M bis (trifluoromethane) sulfonamide lithium salt (LiTFSI, Alfa Aesar) in a mixture of 1,3 dioxolane (DOL, Sigma-Aldrich) and dimethoxyethane (DME, Alfa Aesar) (v/v=1:1) with 2 wt.% lithium nitrate (LiNO_3 , Alfa Aesar) as an additive. The cells were assembled in an Ar-filled glove box with H_2O and O_2 contents less than 0.1 ppm (M-Braun, Germany).

Cycling stability of the S@C hybrids was measured by discharging and charging galvanostatically the cells in a potential range of 3.0–1.0 V vs. Li⁺/Li at a current density of 0.1 C (1 C = 1672 mA g⁻¹) using an electrochemical testing system (Neware Technology Co., China). The rate capability of the S@C hybrids was measured from 0.1 C to 5 C in the same potential range. The specific capacity of the S@C hybrids was calculated on the basis of sulfur mass in the S@C hybrids. Cyclic voltammetry measurements were carried out at a scan rate of 0.1 mV s⁻¹ in a potential range of 3.0–1.0 V vs. Li⁺/Li (MSTAT-1, Arbin). Electrochemical impedance spectra (EIS) were measured in a frequency range of 100 kHz to 0.01 Hz and at a potentiostatic signal amplitude of 5 mV by a frequency response analyzer (1255B solarton) equipped with an electrochemical interface (1287, Solartron). All the electrochemical tests were performed at 25 ± 1 °C.

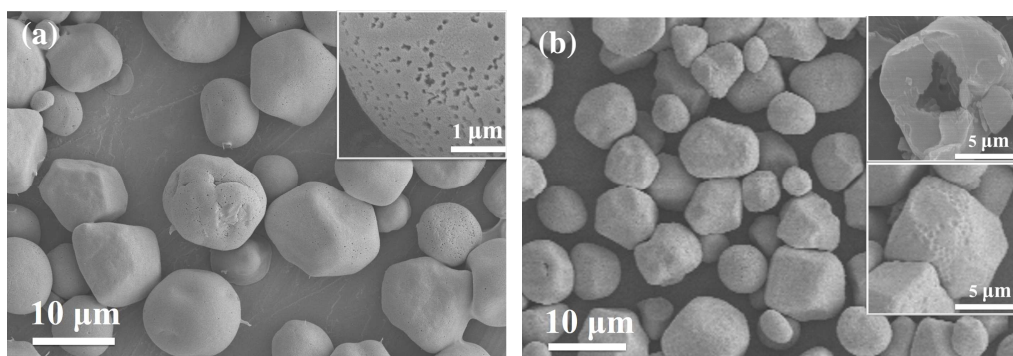
Results and discussion

Structure characterization

XRD analysis (Fig. S2) of the pyrolyzed amylose by the different methods shows that their diffraction patterns are similar. The broad peak at around 23° and the relatively weak peak at around 43°, corresponds to the (002) and (100) reflections of pretended (what does this mean here ???) graphitic domains,^{3,7} demonstrating partial graphitization of the carbon.

Figs. 1a–d show the SEM images of the raw amylose and its carbonized products by multi-step, one-step and KOH etching-assisted pyrolysis,

respectively. The insets are the large magnification images of the corresponding samples to show more details of the particles. As seen from Fig. 1a, the raw amylose powder has a spherical shape with size ranging from 5 to 15 μm , and most of them are of *ca.* 10 μm . Mesopores are observed on the surface of most of the amylose particles, as shown in the inset. The overall morphology of the multi-step pyrolyzed product is similar to that of the raw amylose, but shows reduced particle size as seen from Fig. 1b. Moreover, from the SEM observation of its crushed particle after being freezed in liquid nitrogen, as shown representatively in the top inset of Fig. 1b, it is found that there is macroporous in size of *ca.* 2 – 3 μm inside the particle. The raw amylose particles cannot be crushed even assisted by liquid nitrogen freezing, so their inside structure is failed to be characterized. In addition, most of the mesopores occurring on the surface of the raw amylose particles disappear after the multi-step pyrolysis, but instead showing rough surface, as shown in the bottom inset of Fig. 1b.



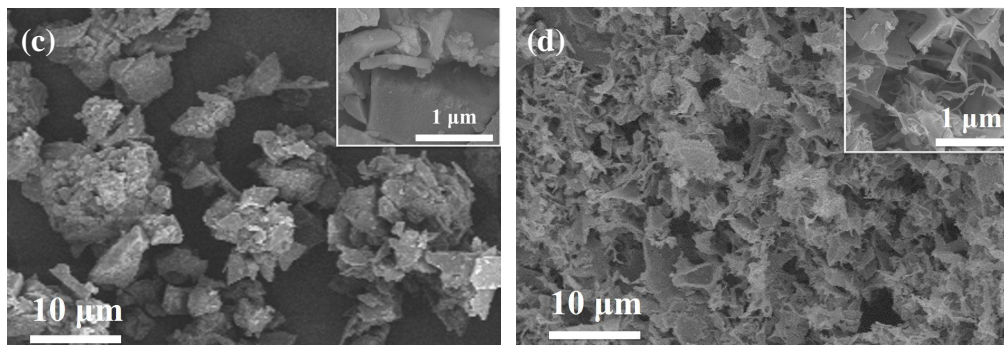


Fig. 1 SEM images of the raw amylose (a) and after multi-step (b), one-step pyrolysis (c) and KOH etching-assisted (d) pyrolysis. The insets are their corresponding large magnification morphologies.

In comparison, the spherical morphology of the raw amylose was completely destroyed after the one-step pyrolysis, showing a typically crushed shape after milling by agate mortar, and no pores are observed by SEM, as shown in Fig. 1c and the inset. The product obtained by KOH etching-assisted pyrolysis shows fluffy spongy-like structure, which is different from either of the multi-step pyrolysis, or the one-step pyrolysis, as shown in Fig. 1d and the inset. KOH can react with carbon, forming potassium carbonate (K_2CO_3) at about 600 °C by the following equation.⁴ K_2CO_3 further decomposes into CO_2 and potassium oxide at temperatures higher than 700 °C.



Figs. 2a and b are the N_2 adsorption isotherms and the pore size distribution curves of the pyrolyzed products, respectively. Fig. 2a shows that all the samples show type I isotherm adsorption according to the Brunauer classification.²⁹ Steep condensation steps occur only when the P/P_0 value is lower than 0.05 and no other condensation steps are observed in the other range. The result indicates that the detected pores of the different samples are mainly

microporous. Fig. 2b shows that the pore size ranges mostly in 1.0–2.0 nm, which are extremely small. Combining the macroporous core inside the spheres (Fig. 1), it is obtained the multi-step pyrolyzed carbon (MHPC) has a hierarchical porous structure with macroporous core and microporous shell, and the one-step pyrolyzed (OSPC) and KOH etching-assisted pyrolyzed carbon (KEAC) has only micropores. Moreover, the MHPC has more amounts of pores than the other two, and the majority of the pores show size of *ca.* 1.2 nm (Fig. 2b). The surface area and pore volume for the differently pyrolyzed carbon are listed in Table 1. As the pores with size larger than 100 nm cannot be measured by the BET method, the macropore inside the MHPC particles are not included in Fig. 2 and their volume is not involved in the value listed in Table 1. As seen in Table 1, the MHPC has a specific surface area of 672.6 m² g⁻¹, which is higher than that of the KEAC (508.2 m² g⁻¹), and is much higher than that of the OSPC (277.6 m² g⁻¹). Even without including the macropores, the volume of the micropores of the MHPC is still the highest among the three types of carbon, being 0.32 cm³ g⁻¹, while those of the OSPC and KEAC are 0.13 and 0.26 cm³ g⁻¹, respectively.

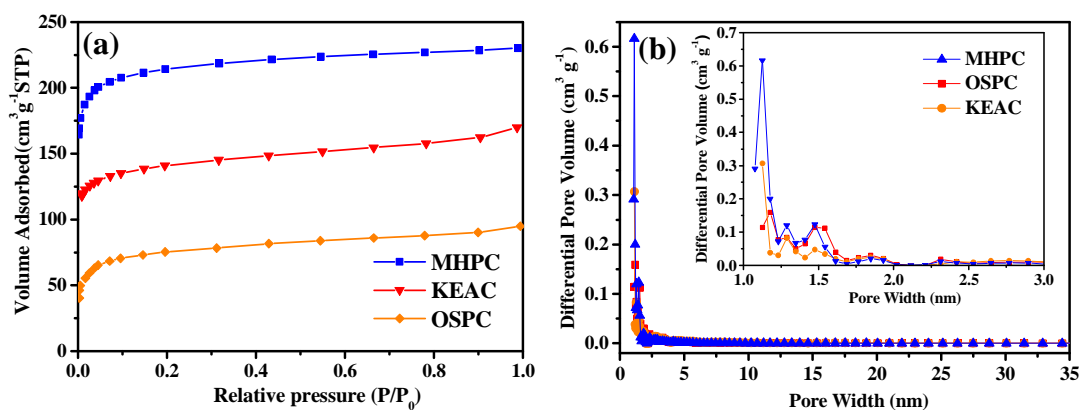


Fig. 2 N₂ sorption isotherms (a) and pore size distribution (b) of the differently pyrolyzed carbon

Table 1 Surface area and pore volume of the differently pyrolyzed carbon and the S@C hybrids

	Surface area (m ² g ⁻¹)	Pore volume (cm ³ g ⁻¹)
MHPC	672.6	0.32*
OSPC	277.6	0.13
KEAC	508.2	0.26
S@MHPC	5.3	0.01
S@OSPC	5.4	0.01
S@KEAC	4.6	0.01

* the volume of the inside macroporous core of the MHPC particles is not involved.

As known from the TG curve of the raw amylose (Fig. S1), vapor of H₂O was highly generated at 260–360 °C. High temperature H₂O vapor has high energy, which damages the micelle structure of amylose molecules and makes amylose into a paste³¹. This is likely the main reason for the low porosity and low surface of the one-step pyrolyzed carbon, where a quick heating (5 °C min⁻¹) up to 900 °C was used. Whereas for the multi-pyrolysis, the low heating rate in the temperature range of 240–350 °C is suggested to lower greatly the evaporation rate of H₂O. The low heating rate, coupled with the high flow rate of the carrying gas, favours greatly the removal of the moisture, and hence reduces the damage of the high energy H₂O vapor on the spherical shape of the original amylose. As a result, the spherical shape of the original amylose is preserved. For the KEAC, due to the strong etching of KOH to carbon, the damaged spherical shape was further carved to fluffy spongy-like structure. The gases (H₂O, CO, CO₂ and H₂, Fig. S1) generated during the pyrolysis process are supposed to be the main factor for the formation of the micropores in the

differently pyrolyzed carbon. The formation of the macroporous core inside the MHPC is also likely to benefit from the low evaporation rate of H₂O vapor and the high flow rate of the carrying gas.

Raman spectra of the differently pyrolyzed carbon and their S@C hybrids are shown in Figs. 3a and b, respectively. The spectra of the differently pyrolyzed carbons look similar. The peak centered at *ca.* 1600 cm⁻¹ is the G band, corresponding to the stretching vibrations in the graphene layer; the peak centered at *ca.* 1350 cm⁻¹ is the D band of carbon, associating with disordered graphite lattices. The ratios of the intensity of D band and G band for the differently pyrolyzed, I_D/I_G , show a similar value of *ca.* 1.7, indicating a short range ordered and long range disordered structure for them (you mean both short and long range orders exist in the structure?). In addition, the MHPC, OSPC and KEAC all show a G' band in the range of 2500–2800 cm⁻¹, corresponding to an overtone of the G band, which occurs commonly in graphitic materials, but not in amorphous carbon.³²⁻³⁴ This confirms the present carbon contains graphitic domains. Such G' band is also reported in a carbonized shaddock peel, showing comparatively ordered graphitic structure.³⁵ Graphitization, even partially, is a substantial prerequisite in improving the conductivity of carbonaceous materials,³² which is helpful in facilitating the transportation of electrons of sulfur during electrochemical cycling.

The D, G and G' bands from carbon also appear in the S@C hybrids. The I_D/I_G value of the different S@C hybrids shows a close value of *ca.* 2.1, which

is slightly higher than that of the original carbon, indicating a decreasing level of order in the structure. Increase of I_D/I_G after impregnating sulfur is also reported in other S/C systems, such as the carbonized 1,4-H₂NDC and sulfur system, where sulfur is reported to interact with the dangling bonds of carbon, resulting in extended sp² C-C bonds.³⁶ In addition, sulfur is not detected by the Raman measurement, indicating that individual sulfur should be mostly removed during the extra heating at 300 °C for 0.5 h after the sulfur infiltration process, and there is also extremely limited sulfur exposed on the surface of the S@C hybrid particles.

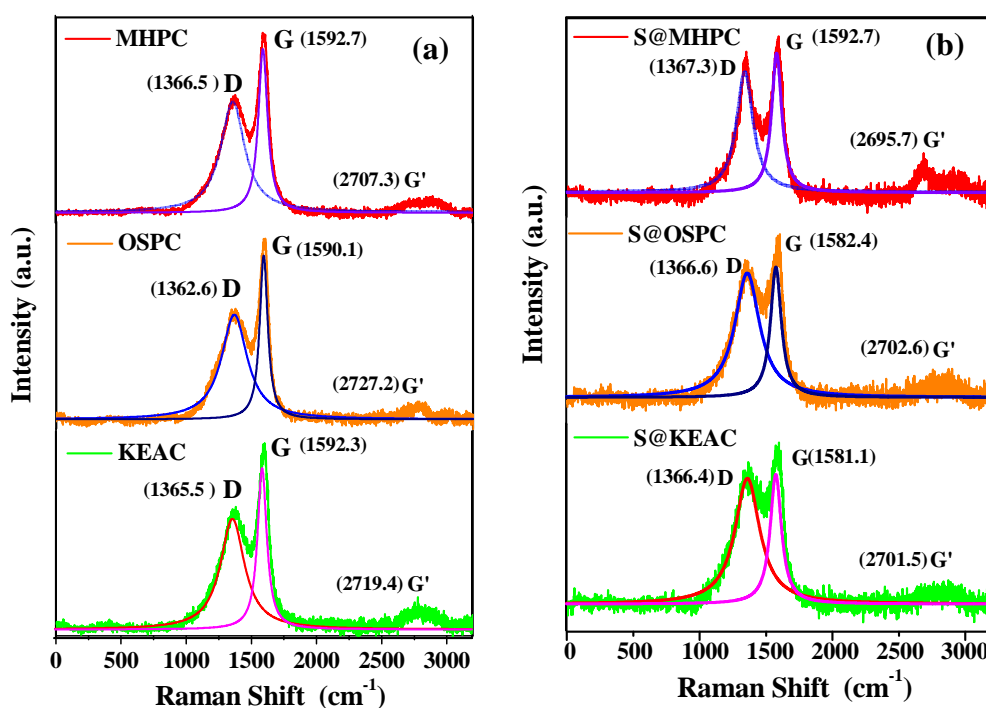


Fig. 3 Raman spectra of the three types of carbon (a) and the three S@C hybrids (b).

Though sulfur is not detected by Raman analysis, XRD analysis of the S@MHPC, S@OSPC, S@KEAC hybrids (Fig. S3) shows that there are strong sulfur diffraction peaks in all the patterns of the S@C hybrids, which are highly

identical to orthorhombic sulfur (JCPDS 08-0247). No visible difference is observed between the diffraction peaks of sulfur in the hybrids and those of the pristine sulfur. The diffraction peaks of sulfur are all very sharp, indicating a highly crystallized structure. The hump peaks from carbon (Fig. S2) are not observed in the patterns of the S@C hybrids, which is probably due to the lowered crystallization of the carbon after sulfur incorporation as shown in the Raman measurement.

The SEM morphology of the S@MHPC hybrid is shown in Fig. 4a. The insert of Fig. 4a is a schematic structure of the S@MHPC hybrid particle. Comparison of Fig. 4a and Fig. 1a shows that the size of the S@MHPC hybrid is not visibly different from that of the original MHPC particles. The spherical shape and the size of the MHPC particles are well retained after incorporating with sulfur. Congregated sulfur as reported in a sulfur/porous carbon fiber composite³⁷ is not found in the S@MHPC hybrid. It is confirmed that congregated sulfur should be removed mostly after the extra heating at 300 °C for 30 min in flow argon. In addition, different from the rough surface of the MHPC particles, the surface of the S@MHPC particles looks smooth. A thin coating of sulfur absorbed tightly on the rough surface of the MHPC particles is also reasonable. Such micron-sized spherical S@C hybrid with different sizes is hopefully favorable in getting high-tap density and hence the volumetric density of the batteries, which is important for practical applications. Fig. 4b shows representatively a crushed S@MHPC particle (the left) and its EDS

mapping of sulfur (the right). It is seen that the macroporous core in the MHPC particles still maintains in the S@MHPC hybrid. The macroporous core is not fully filled with sulfur after the sulfur immersion process. It indicates that the long and narrow channels in the thick shell do not facilitate the flow of sulfur. However, Fig. 4b shows that sulfur is evenly distributed in the particle shell, indicating fully filled micropores. Fig. 4c and d shows the morphologies of the S@OSPC and S@KEAC hybrids, respectively, which also seem similar to their original carbon (Fig. 1c and d), indicating that sulfur exists mostly in the micropores of the OSPC and KEAC also. Further EDS analysis also shows that sulfur is evenly distributed in the S@MHPC, S@OSPC and S@KEA hybrids (Fig. S4).

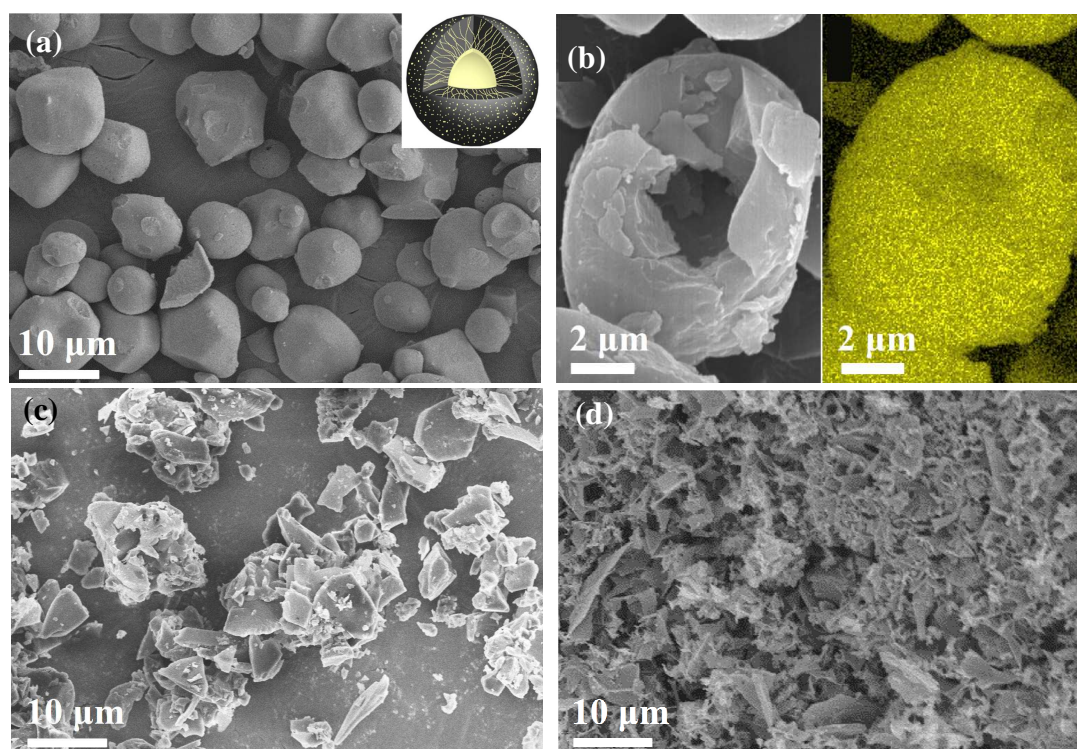


Fig. 4 SEM morphologies of the S@MHPC hybrid (a), a representative crushed S@MHPC particle (left) and its EDS mapping of sulfur (right), S@OSPC(c) and S@KEAC (d) hybrids. The insert of Fig. 4a is a schematic structure of the S@MHPC hybrid particle.

The TG and the derivative weight loss curves of the S@C hybrids are shown in Fig. 5. The weight loss is attributed to the evaporation of sulfur. It is seen that the onset evaporation temperature of sulfur in the hybrids are all higher than that of the individual one. Among them, the S@MHPC hybrid shows the highest onset evaporation temperature of 190 °C, which is *ca.* 30 °C higher than that of the individual sulfur. In addition, it is clear that the S@MHPC hybrid shows a two-step evaporation process, indicating that there are different evaporation characteristics. The first step of the S@MHPC hybrid takes place at 250–350 °C and centers at *ca.* 295 °C, corresponding to a weight loss of 15 wt%. The second step takes place at 350–510 °C and centers at *ca.* 480 °C, corresponding to a weight loss of 22 wt%. A totally stable value of 47 wt% is obtained. Moreover, it is seen that the evaporation of sulfur at the high temperature range is much slower than that at the low temperature range. It is probably that sulfur confined in the much deep micro-channels of the S@MHPC is much difficult to evaporate. While both S@OSPC and S@KEAC hybrids show only one-step evaporation, centering at *ca.* 250 °C and 290 °C, and finishing at *ca.* 280 °C and 335 °C, respectively, all at lower temperatures than the S@MHPC hybrid. The total weight loss of the S@OSPC and S@KEAC hybrids, which are the S contents of the hybrids, are 24 wt% and 37 wt%, respectively. Both are lower than that of the S@MHPC. The depth of the micro-channels of the OSPC and KEAC particles is shallower than that of the MHPC particles. As shown in Fig. 4, at least, the S@OSPC and S@KEAC

hybrids show an overall smaller particle size than the S@C hybrid. In comparison, individual sulfur evaporates quickly and the evaporation ends at *ca.* 310 °C. So far, it is obtained that there is effective interaction between the confined S and carbon substrate for all the hybrids.

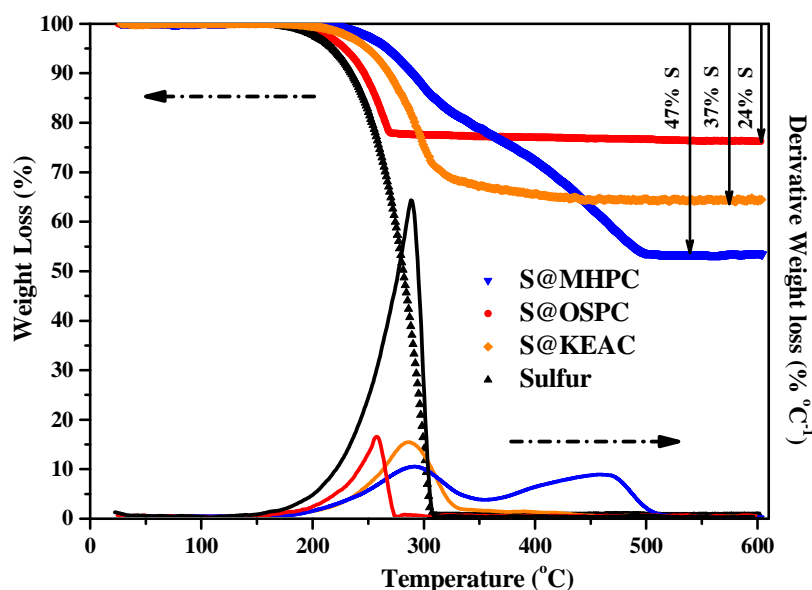


Fig. 5 TG and the derivative weight loss curves of the S@C hybrids prepared from the differently pyrolyzed carbon.

The calculated amount of sulfur that the micropores in the MHPC particles can accommodate based on the porosity of the MHPC (Table 1), taking the densities of the MHPC and sulfur to be 1.39 and 2.07 g cm⁻³, respectively, are 40 wt.%, which is 7 wt% lower than the S content of the S@MHPC hybrid detected by TG analysis (47 wt.%). It is likely that there is also some amount of sulfur filled in the macropore inside the MHPC and absorbed on the surface of the MHPC particles, though there is still a macropore in the S@MHPC particles (Fig. 4b). The sulfur contents that the micropores in the OSPC and KEAC can accommodate calculated by the same way are 22 wt.% and 35 wt.%, respectively, which are very close to the values detected by TG analysis (24

wt% and 37 wt%). The TG data of the sulfur impregnated S@C systems without the extra heating at 300 °C after the sulfur immersion process are shown in Fig. S5. It is seen that the weight loss of the three systems shows a similar value of 56–57 wt.%, which are all slight lower than the added content of sulfur due to lose during the sulfur immersion process, but they are all higher than the sulfur contents in the S@C hybrids, confirming the removing of the free sulfur during the extra heating at 300 °C after the sulfur immersion process.

The surface area and the pore volume of the S@C hybrids are also listed in Table 1, which show largely reduced values, compared with those of the original carbon hosts. The S@C hybrids show close values of only 4.6–5.4 g cm⁻³ for the surface area and a same value 0.01 cm³ g⁻¹ for the pore volume. The results confirm that the micropores in the carbon hosts are mostly filled with sulfur.

Electrochemical properties

Fig. 6a shows the cycling stability and the Coulombic efficiency at 0.1C of the S@MHPC, S@OSPC and S@KEAC hybrids. The S@MHPC hybrid exhibits an initial discharge capacity of 1490 mA h g⁻¹ at 0.1 C, which is 88% of the theoretical capacity of sulfur and retains a capacity of 798 mA h g⁻¹ up to 200 cycles, corresponding to the capacity retention of 54%. In addition, the Coulombic efficiency decreases from 99% for the first cycle to 95% after several cycles, and then maintains at 95% in the subsequent cycles, which is

supposed due to the weakly trapped sulfur on the surface of the S@MHPC hybrid was easily dissolved in the electrolyte at the initial several cycles. The degradation of the capacity and Coulombic efficiency in the first several cycles is severer, however, the capacity fading is stable when the weakly trapped sulfur was consumed.

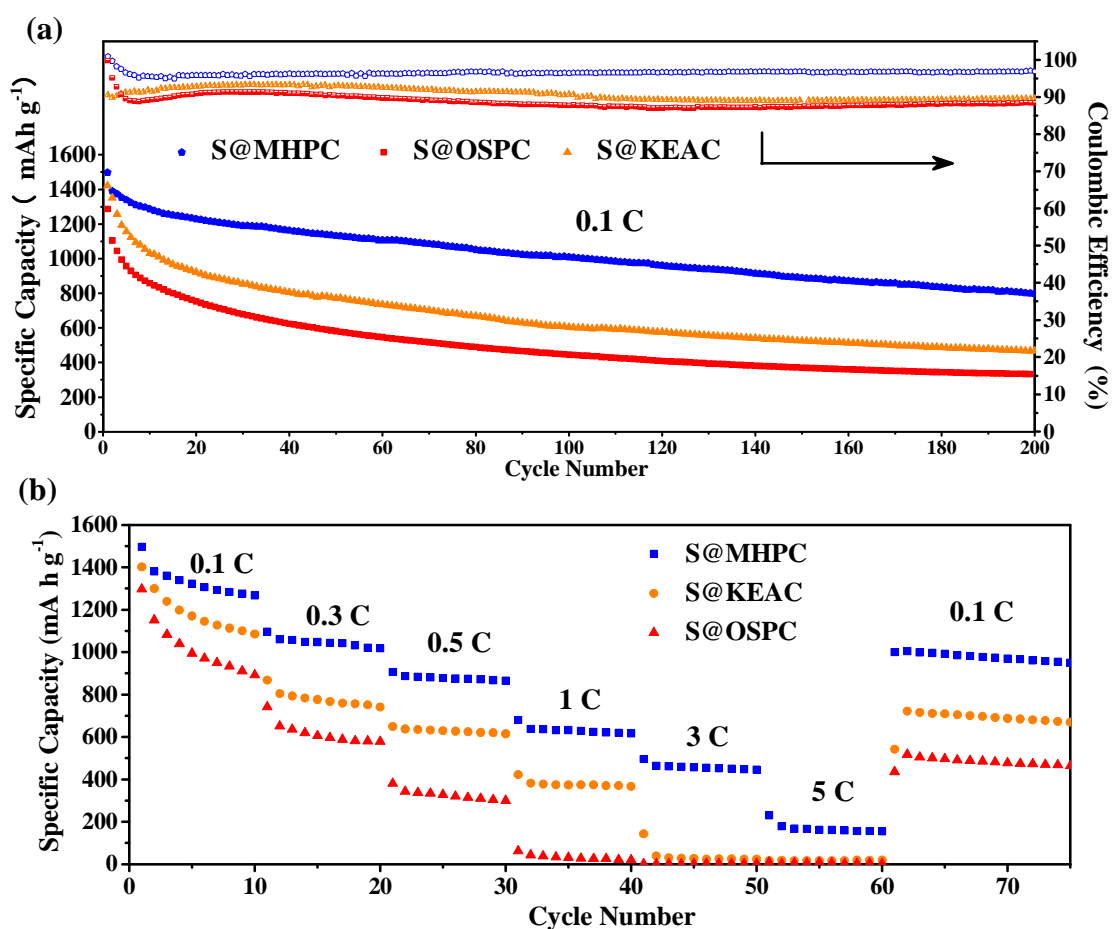


Fig. 6 Cycling stability at 0.1C (a) and rate capability (b) of the S@MHPC, S@OSPC and S@KEAC hybrids.

In comparison, the S@OSPC hybrid shows an initial discharge capacity of 1280 mA h g⁻¹, which is over 200 mA h g⁻¹ lower than that of the S@MHPC hybrid. The capacity after 200 cycles is only 367 mA h g⁻¹, corresponding to the capacity retention of only 27%, much severer capacity fading than that of the S@MHPC hybrid, especially in the initial several cycles as seen from Fig. 6a,

implying low sulfur utilization with severe polysulfide dissolution. It is obtained that the micron-sized spherical hierarchical porous structure with high porosity of the MHPC is much beneficial in trapping sulfur than that of the OSPC. The initial capacity, initial Coulombic efficiency and the capacity retention after 200 cycles of the S@KEAC hybrid are 1421 mA h g⁻¹, 89% and 33%, respectively, which are all lower than those of the S@MHPC hybrid, but higher than those of the S@OSPC hybrid. The Coulombic efficiency of the S@OSPC and S@KEAC hybrids upon cycling is several percentages lower than that of the S@MHPC hybrid, showing an relatively lower stable value ranging in 87–93% as overall.

Fig. 6b shows the rate capability of the S@C hybrids at 0.1 C up to 5 C. It is seen that the capacities of the S@MHPC hybrid at 0.5 C, 1 C, 3 C and 5 C are 907, 681, 487 and 226 mA h g⁻¹, respectively, which are all much higher than those of the S@OSPC and S@KEAC hybrids. Due to the high ohmic and kinetic over potential at high rate, the capacity decrease with increasing current rate. In addition, a capacity of 1000 mA h g⁻¹ is recovered when the current density is returned back to 0.1 C, which is still high, though there is capacity degeneration after cycling at different rates. In comparison, the S@OSPC hybrid fails to cycle at 1 C and its capacity at 0.5C is only 380 mA h g⁻¹. The S@KEAC hybrid fails to cycle at 3 C and its capacity at 1C is only 420 mA h g⁻¹.

The significantly improved capacity, cyclic stability and high-rate

capability of the S@MHPC hybrid is due to its unique structure: the inner macropore can accommodate the volume change of the lithium polysulfide in the micro-channels in the shell; the long and narrow micro-channels in the shell not only confine and sequester sulfur and its transformed polysulfides, preventing effectively the dissolution of the polysulfides in the electrolyte, but also maintain an intimate contact of sulfur and polysulfides to the carbon substrate, providing sufficient electron conductivity for the hybrid; the large surface area and high porosity provide more sites for loading insulating $\text{Li}_2\text{S}/\text{Li}_2\text{S}_2$ and favor the lithium-ion transportation; the partial graphitization offers high electron conductivity. However, for the OSPC and KEAC, the superiority is not so sufficient, therefore, the S@OSPC and S@KEAC hybrids show inferior electrochemical properties to the S@MHPC hybrid.

Although the electrochemical properties of the S@C hybrids from different laboratories cannot be quantitatively compared because of different electrode preparation and testing programs, it is still useful to observe progress made among the research communities. Comparison of the capacity and cyclic performance of the present S@MHPC hybrid with those of the typically reported sulfur cathode using other carbonized biomass hosts that we find is shown in Table 2. It is seen that the initial discharge capacity and the capacity retention after 100 cycles at 0.1 C of the present S@MHPC hybrid are much higher than those of the S@shaddock peel⁷ system. The initial discharge capacity and the capacity after 200 cycles at 0.1 C of the S@MHPC hybrid are

also much higher than those of the S@cotton⁴ and S@apricot shell⁵ system which are also cycled for 200 cycles but at 0.2 C. If the magnitude of the present capacities at 0.1 C cannot be quantitatively compared with the reported values at a higher rate of 0.2 C, however, it is seen that the capacity retention of the present S@MHPC hybrid at 0.1 C after 200 cycles is very close to those of the S@apricot shell system at 0.2 C after 200 cycles⁵ and the S@silk cocoon system at 0.5 C after 80 cycles.⁶ Though the present capacity retention of the S@MHPC hybrid at 0.1 C after 200 cycles seems lower than that of the S@cotton system after 200 cycles also but at 0.2 C,⁴ it is noted that its initial capacity is somewhat lower than the reported S@apricot shell system⁵ at the same rate of 0.2 C, which favors capacity retention. It is different (difficult ?) to compare the cyclic stability of the present S@MHPC hybrid with the S@bamboo charcoal²⁵ system, as a rate of 0.5 C is used and 500 cycles are tested for the later. However, the capacity of 907 mA h g⁻¹ of the present S@MHPC hybrid at 0.5 C after cycled at 0.1 C and 0.3 C, respectively, for each 10 cycles (Fig. 6b), is much higher than the initial capacity of 685 mA h g⁻¹ for the S@bamboo charcoal system at 0.5 C. Moreover, the capacity of 681 mA h g⁻¹ at 1C of the present S@MHPC hybrid (Fig. 6b) is comparable to that of the S@cotton system,⁴ and is higher than the 640 mA h g⁻¹ for the S@apricot shell,⁵ the 500 mA h g⁻¹ for the S@shaddock peel⁷ and the 481 mA h g⁻¹ for the S@bamboo charcoal systems.

It is clear that the present S@MHPC hybrid has demonstrated superior

capacity, capacity retention and rate capability, compared with most of the other reported S@C hybrids with biomass derived carbon. The special surface area of the present MHPC ($672 \text{ m}^2 \text{ g}^{-1}$) is not so high as those of the cotton ($1286 \text{ m}^2 \text{ g}^{-1}$),⁴ apricot shell ($2269 \text{ m}^2 \text{ g}^{-1}$),⁵ S@silk cocoon ($3243 \text{ m}^2 \text{ g}^{-1}$)⁶ and shaddock peel ($937 \text{ m}^2 \text{ g}^{-1}$)⁷ derived carbon, the long and narrow channels in the spherical shell are likely to confine sulfur, preserving the polysulfide from dissolving in the electrolyte, resulting less shuttle effect and offering a high electrical conductive contact of the active material with the carbon substrate. The sulfur content in the present work is comparable to those of the S@apricot shell⁵ and S@silk cocoon⁶ systems, but is somewhat lower than those of the S@cotton,⁴ S@shaddock peel⁷ and S@bamboo charcoal²⁵ systems. Exploring the way to fill a higher amount of sulfur to the macroporous cores inside the MHPC particles is expected in the future work to increase the sulfur content of the S@MHPC hybrid.

Table 2 Electrochemical performance of the S@C cathodes based on different biomass derived porous carbon

Carbonized biomass materials	Current rate*	Initial capacity (mA h g ⁻¹)	Cycle number**	Sulfur content (%)	Capacity retention ratio (%)	Capacity at the noted number (mA h g ⁻¹)	Refs.
HPC	0.1	1490	200	48	54	798	Our work
HPC	0.1	1490	100	48	68	1015	Our work
Cotton	0.2	1017	200	68	75	760	4
Apricot shell	0.2	1277	200	53	56	710	5
Silk cocoon	0.5	1443	80	48	56	804	6

Shaddock peel	0.1	1190	100	62	55	179	7
Bamboo charcoal	0.5	685	500	58	60	414	25

** The cycle rates in the Table are those used for testing cycling performance in the references

*The cycle numbers in the Table are the reported maximum numbers in the references.

Fig. 7a–c shows the discharge/charge profiles of the different S@C hybrids with a cut-off potential of 1–3 V vs. Li⁺/Li of selected cycles at 0.1 C. It is seen that all the hybrids show mainly two discharge plateaus and one charge plateau. The discharge plateau at the comparatively high potential range, corresponding to the transition of elemental sulfur to long-chain polysulfides (Li₂S_x, 4 ≤ x ≤ 8), drops slightly upon the discharge process, which indicates that the transition is partially affected by the diffusion of lithium ions. The plateau at the comparatively low potential range, corresponding to the further reduction of the polysulfides to Li₂S₂/Li₂S are flat, especially for the S@MHPC hybrid, indicating that the reduction occurs at a considerably stable potential, which is almost diffusion-independent. The latter process generates more capacity than the former, which is a major process. For the S@MHPC hybrid (Fig. 7a), the discharge plateau is slightly lowered by *ca.* 0.05 V after initial several cycles, and turns to recover with the further cycling and maintains almost stable up to the tested 200 cycles. However, the discharge plateaus of the S@OSPC and S@KEAC hybrids shift gradually to low potential upon cycling, indicating an increasing reduction polarization. The charge plateau represents the reverse reaction from Li₂S₂/Li₂S to polysulfides and finally to sulfur, or to Li₂S₈ if the oxidation is insufficient. The initial charge plateaus for all the three S@C

hybrids are considerably flat. However, only the S@MHPC hybrid maintains a flat and stable potential upon cycling up to 200 cycles, while the S@OSPC and S@KEAC hybrids all show increasing sloping plateaus upon cycling, indicating an increasing polarization with a sluggish oxidation.

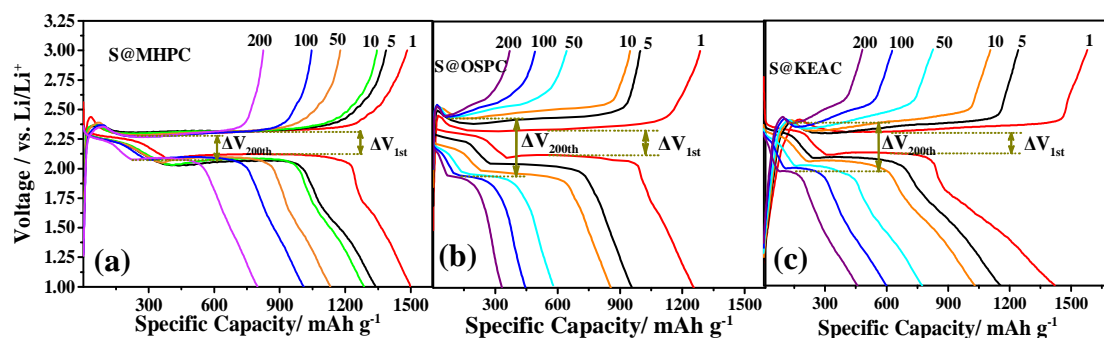


Fig. 7 Charge-discharge profiles of the S@MHPC, S@OSPC and S@KEAC hybrids of selected cycles at 0.1 C.

The overpotential, the potential gap between charge (oxidation) and the main discharge (reduction) plateaus (ΔV as shown in Fig. 7a–c), of the S@MHPC hybrid shows an almost stable value of 0.20 V for the first cycle and the 200th cycle as obtained from the redox peak differences of the differential capacity to potential of the discharge/charge curves (dQ/dV curves, Fig. S6a, b), suggesting an efficient kinetic reaction process with a small barrier. The overpotentials of the S@OSPC and S@KEAC hybrids in the initial cycle are not evidently difference from that of the S@MHPC hybrid, which are 0.22 V and 0.21 V, respectively. However, the values increase to 0.51 V and 0.43 V, respectively, for the S@OSPC and S@KEAC hybrids at the 200th cycle (Fig. S6c, d and e,f). The polarization becomes much severer upon cycling, especially for the S@OSPC hybrids. In addition, as seen from Fig. 7b and c, the

increase of the overpotentials of the S@OSPC and S@KEAC hybrids takes place mainly in the initial several cycles. The overpotential increases very limitedly from the 50th cycle to the 200th cycle as shown in Figs. 7b and c, indicating a stable tendency of electrochemical reaction upon cycling. It is confirmed that the unique hierarchical porous structure of the MHPC alleviates effectively polysulfide from dissolving into the electrolyte, and hence there would be less poorly conductive discharge product of Li₂S/Li₂S₂ generated on the electrode surface. The high surface area and high porosity of the MHPC also allows more sites for the deposition of the insulating Li₂S/Li₂S₂ and allows facile lithium-ion transportation. As a result, the S@MHPC hybrid keeps a low polarization during cycling.

The overpotentials of the S@C hybrids at high current rates, which are obtained from the redox peak differences of the dQ/dV curves (Fig. S7–9) of the first cycle at that rate, the discharge capacities of which are shown in Fig. 6b, are illustrated in Fig. 8. As the S@OSPC hybrid failed to cycle over 0.5 C and the S@KEAC hybrid failed to cycle over 1C, their overpotentials are only obtained up to 0.5 C and 1C, respectively. As seen from Fig. 8, the overpotential increases evidently with the rate, and the differences among the different hybrids enlarge with the current rate. The overpotential of the S@MHPC hybrid increases slightly from 0.20 V at 0.1 C to 0.22 V at 0.5 C, while that of the S@OSPC hybrid increases evidently from 0.22 V at 0.1 C to 1.0 V at 0.5 C. The overpotential of the S@MHPC hybrid is only 0.32 V at 1 C

and 0.62 V at 3 C, which are all lower than that of the S@OSPC hybrid at 0.5 C. The value is only 1.0 V for the S@MHPC hybrid even at a high rate of 5 C, the same as that of the S@OSPC hybrid at 0.5 C. The overpotentials of the S@KEAC hybrid are always in between the values of the S@OSPC and S@MHPC hybrids at the corresponding rate. The above result suggests further that the spherical hierarchical porous structured carbon is beneficial in improving kinetic performance of the sulfur cathode.

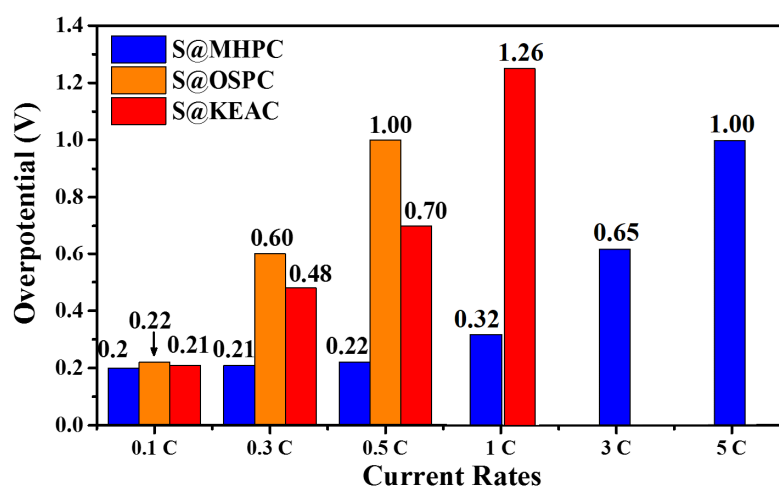


Fig. 8 Overpotentials of the S@MHPC, S@OSPC and S@KEAC hybrids (with respective of the delithiation and the main lithiation of polysulfide to $\text{Li}_2\text{S}_2/\text{Li}_2\text{S}$) at different rates.

Fig. 9a–c shows the cyclic voltammetry (CV) plots of the initial five cycles of the S@C hybrids. For the S@MHPC hybrid, as seen from Fig. 9a, there are two major peaks centering at *ca.* 2.28 and 2.03 V (vs. Li^+/Li) in the first cathodic sweep, corresponding to the transition from elemental sulfur to polysulfides (Li_2S_x , $4 \leq x \leq 8$) and the further reduction of the polysulfides to $\text{Li}_2\text{S}_2/\text{Li}_2\text{S}$ as common, respectively, which is in agreement with the two discharge plateaus in Fig. 7a. The two minor peaks centering at 1.68 and 1.40 V in the first cathodic sweep are attributed to the irreversible reduction of

LiNO₃.^{38, 39} Similar peaks also appear in the S@OSPC and S@KEAC hybrids, as seen in Fig. 9b and c. In the first anodic sweep, there is a strong and sharp peak centering at *ca.* 2.48 V, attributed to the conversion of Li₂S/Li₂S₂ to Li₂S₈/S₈, which is also consistent with the main charge plateau in Fig. 7a. Because of the hysteresis in the CV technique,⁴⁰ the cathodic peaks shift to a lower potential and the anodic peak shift to a higher potential compared to the discharge/charge plateau potentials. There is a weak shoulder peak centering at *ca.* 2.69 V, which is considered from the conversion from Li₂S₈ to sulfur.⁴¹ The cathodic peak corresponding to the transition from sulfur to the polysulfides shifts slight from 2.28 V to 2.32 V after 5 cycles. Moreover, the main anodic peak shows a ignorable shifts from 2.48 to 2.47 V after 5 cycles. In addition, the position of the peak relating to the reduction of polysulfide to Li₂S₂/Li₂S almost does not change upon cycling. Overall, the polarization of the S@MHPC hybrid shows relatively a stable low level in the tested cycles, which is attributed to the well encapsulated sulfur in the spherical microporous carbon shell and hence less amount of polysulfides dissolving in the electrolyte. As a result, there is less amount of insulating Li₂S/Li₂S₂ depositing on the electrode, and there is also intimate contact of S/polysulfides with the carbon substrate, which favor both electron transfer and lithium-ion diffusion.

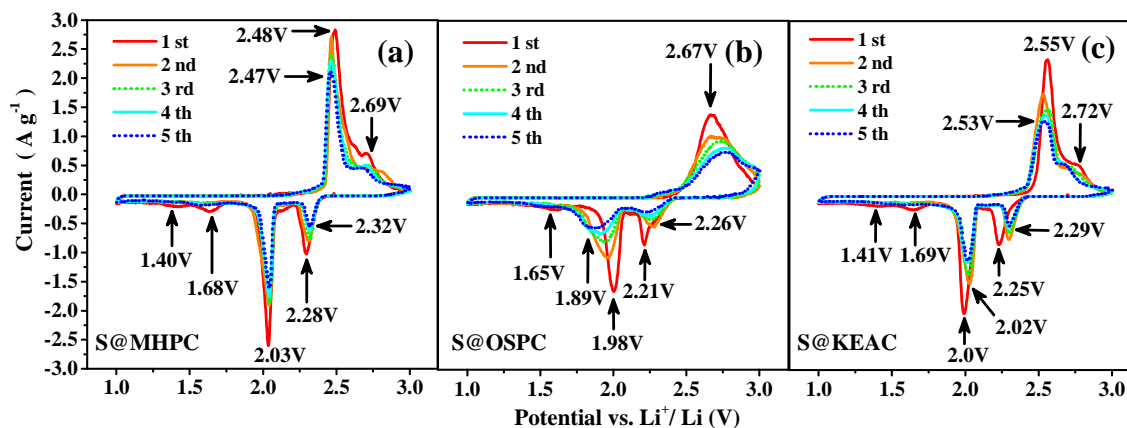


Fig. 9 CV profiles of the S@MHPC (a), S@OSPC(b) and S@KEAC(c) hybrids.

In comparison, there are also two major cathodic peaks in the CV curves of the S@OSPC hybrid, but center at lower potentials (1.98 and 2.21 V) and are much broader than those of the S@MHPC hybrid. There is also only one anodic peak appearing, centering at *ca.* 2.67 V, but is broad. The peak potential is higher than that of the S@MHPC hybrids (2.48 V). The larger redox overpotential and broader peak indicate larger redox polarization and lower redox kinetics, which is in agreement with that obtained from the discharge/charge plateaus (Fig. 7b). The weak shoulder peak occurring at 2.69 V for the S@MHPC hybrid cannot be observed in Fig. 9b. It is probably overlapped by the broad peak or there is no such peak. One anodic peak without coupling a weak shoulder peak is commonly found in S@C systems, such as graphene oxide/sulfur cathode,⁴² porous carbon nanofibers/sulfur cathode.^{37, 43} In addition, One main anodic peak coupling with a weak shoulder peak at higher potential ranging in 2.6–2.8 V is also observed in some other S@C systems, such as S@porous hollow carbon cathode,¹³ dual coaxial nanocable sulfur cathode⁴¹ and nanostructured sulphur-carbon nanotube cathode,⁴⁴ which

is suggested due to the further oxidation of Li_2S_8 to elemental S after the main oxidation of $\text{Li}_2\text{S}/\text{Li}_2\text{S}_2$ to Li_2S_8 , when a high conductive carbon matrix is applied. In this case, it confirms that the highly porous hierarchical structure of the MHPC facilitates electron transfer due to the homogenous distribution of sulfur in the microporous shell and the intimate contact of sulfur to the carbon substrate. Moreover, the overpotential of the redox peaks of the S@OSPC hybrid increases evidently during cycling, indicating a severe increasing polarization, consistent with the result from the discharge/charge profiles (Fig. 7b).

For the S@KEAC hybrid (Fig. 9c), the two main cathodic peaks also locate at higher potentials and the main anodic peak locates at lower potentials compared with those of the S@MHPC hybrid, but the shifts are slightly smaller than those of the S@OSPC hybrid. The weak shoulder peak corresponds to the reduction of Li_2S_8 to S_8 also occurs, which is at 2.72 V. It is obtained that the spongy-like porous structure is superior to the OSPC in reaction kinetics, but is inferior to the MHPC.

Fig. 10 is the Nyquist plots of the S@MHPC, S@OSPC and S@KEAC hybrids. The solid symbols denote the experimental data, and the lines represent the fitting results from the calculation based on the equivalent circuit inserted in Fig. 10. Fig. 10 shows that every spectrum is composed of a semicircle at the high-to-medium frequency region and an inclined line in the low frequency region. The intercept of the semicircle on the real axis at the high frequency is

ascribed to the ohmic resistance resulting from electrolyte, electrode and separator, which is denoted as R_s . The semicircle correlates the charge transfer resistance (R_{ct}) at the interface of the active material and electrolyte. The inclined line represents the Warburg impedance, associated with lithium-ion diffusion in the electrode particles.^{45, 46} Obtained from the fitting result, the S@MHPC hybrid shows a R_{ct} value of 19 Ω , which is lower than the 136 Ω for the S@OSPC hybrid and the 30 Ω for the S@KEAC hybrid. The much smaller R_{ct} value of the S@MHPC hybrid indicates a much higher electronic conductivity and a much higher reaction kinetics. The result further demonstrates that the macroporous core and microporous shell structure of the spherical carbon provides better electronic connection of the incorporated sulfur and the carbon substrate than the structures of the other two types of carbon.

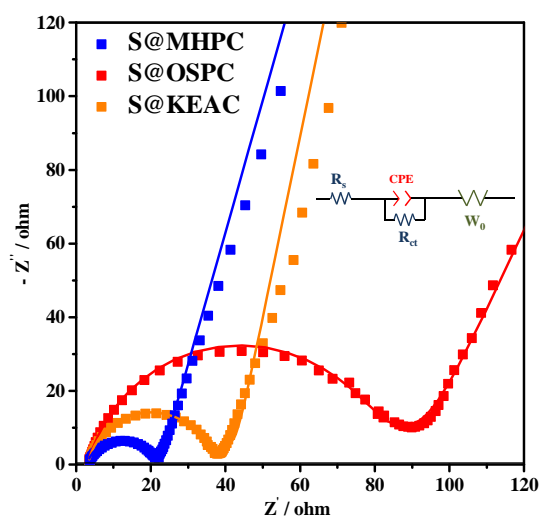


Fig. 10 Nyquist plots of the different S@C hybrids.

Conclusions

A micron-sized spherical carbon with hierarchically macroporous core and microporous shell with a surface area of 672 m² g⁻¹ is successfully synthesized

from a sustainable biomass material of amylose by a multi-step pyrolysis. After incorporating sulfur with melting infiltration, the long and narrow channels in the shell are fully filled with sulfur, but the macroporous core is mostly maintained. This S@C hybrid with a sulfur contents of 48 wt% shows a high initial capacity of 1490 mA h g⁻¹ at 0.1 C and a capacity of 798 mA h g⁻¹ after 200 cycles as cathode material for lithium-sulfur batteries. Capacities of 681 and 487 mA h g⁻¹ is obtained at 1 C and 3 C rates, respectively. This S@C hybrid also shows low polarization and high redox kinetics during cycling.

It is obtained that sulfur is well confined in the long and narrow channels of the spherical carbon, alleviating effectively the dissolution of polysulfides to the electrolyte and offers intimate contact of the active material with the carbon substrate. The large surface area provides sufficient sites for the deposition of the insulating Li₂S₂/Li₂S. The unique structure offers both facile electron transfer and lithium-ion diffusion. The synthesis process does not need any assisted chemical solution, which is considered environmentally friendly. While the one-step pyrolysis and the chemical reagent assisted pyrolysis methods are found only to produce inferior structured porous carbon, which offer inferior electrochemical properties after incorporating sulfur. The multi-step pyrolysis method and the synthesized spherical hierarchically porous carbon is considered having potential application in developing carbonaceous materials from biomass materials for energy storage.

Acknowledgments

The work was supported by the National Natural Science Foundation of PR China (Nos. 51571178, 51571175 and 51371158), National Materials Genome Project (No. 2016YFB0700600), Natural Science Foundation of Zhejiang Province (No. LY14E010004), Pao Yu-Kong International Fund, Zhejiang University and the UK EPSRC (Nos. EP/K002252/1 and EP/K021192/1).

References

1. S. Dutta, A. Bhaumik and K. C. W. Wu, *Energy & Environmental Science*, 2014, **7**, 3574-3592.
2. G. Xu, J. Han, B. Ding, P. Nie, J. Pan, H. Dou, H. Li and X. Zhang, *Green Chem.*, 2015, **17**, 1668-1674.
3. W. Lv, F. Wen, J. Xiang, J. Zhao, L. Li, L. Wang, Z. Liu and Y. Tian, *Electrochimica Acta*, 2015, **176**, 533-541.
4. H. Wang, Z. Chen, H. K. Liu and Z. Guo, *RSC Adv.*, 2014, **4**, 65074-65080.
5. K. Yang, Q. Gao, Y. Tan, W. Tian, L. Zhu and C. Yang, *Microporous and Mesoporous Materials*, 2015, **204**, 235-241.
6. B. Zhang, M. Xiao, S. Wang, D. Han, S. Song, G. Chen and Y. Meng, *Acs Applied Materials & Interfaces*, 2014, **6**, 13174-13182.
7. S. Lu, Y. Chen, J. Zhou, Z. Wang, X. Wu, J. Gu, X. Zhang, A. Pang, Z. Jiao and L. Jiang, *Scientific reports*, 2016, **6**, 20445.
8. A. Manthiram, Y. Z. Fu and Y. S. Su, *Accounts Chem. Res.*, 2013, **46**, 1125-1134.
9. J.-Q. Huang, Q. Zhang, H.-J. Peng, X.-Y. Liu, W.-Z. Qian and F. Wei, *Energy & Environmental Science*, 2014, **7**, 347.
10. X. Ji and L. F. Nazar, *Journal of Materials Chemistry*, 2010, **20**, 9821.
11. Y. X. Yin, S. Xin, Y. G. Guo and L. J. Wan, *Angewandte Chemie*, 2013, **52**, 13186-13200.
12. J. Nelson, S. Misra, Y. Yang, A. Jackson, Y. Liu, H. Wang, H. Dai, J. C. Andrews, Y. Cui and M. F. Toney, *Journal of the American Chemical Society*, 2012, **134**, 6337-6343.
13. N. Jayaprakash, J. Shen, S. S. Moganty, A. Corona and L. A. Archer, *Angewandte Chemie*, 2011, **50**, 5904-5908.
14. G. Zhou, Y. Zhao and A. Manthiram, *Advanced Energy Materials*, 2015, **5**.
15. B. Zhang, X. Qin, G. R. Li and X. P. Gao, *Energy & Environmental Science*, 2010, **3**, 1531.
16. C. Tang, B. Q. Li, Q. Zhang, L. Zhu, H. F. Wang, J. L. Shi and F. Wei, *Advanced Functional Materials*, 2015, **26**.
17. J. Guo, Y. Xu and C. Wang, *Nano letters*, 2011, **11**, 4288-4294.
18. X. Ye, J. Ma, Y. S. Hu, H. Wei and F. Ye, *Journal of Materials Chemistry A*, 2015, **4**.
19. H. Wang, Y. Yang, Y. Liang, J. T. Robinson, Y. Li, A. Jackson, Y. Cui and H. Dai, *Nano letters*, 2011, **11**, 2644-2647.
20. J. Song, Z. Yu, M. L. Gordin and D. Wang, *Nano letters*, 2016, **16**, 864-870.
21. F. Wu, J. Chen, R. Chen, S. Wu, L. Li, S. Chen and T. Zhao, *The Journal of Physical Chemistry C*, 2011, **115**, 6057-6063.
22. W. Qin, B. Fang, S. Lu, Z. Wang, Y. Chen, X. Wu and L. Han, *Rsc Advances*, 2015, **5**, 13153-13156.
23. Q. Zhao, X. Hu, K. Zhang, N. Zhang, Y. Hu and J. Chen, *Nano Letters*, 2015, **15**, 721-726.
24. G. Li, J. Sun, W. Hou, S. Jiang, Y. Huang and J. Geng, *Nature Communications*, 2016, **7**.
25. J. J. Cheng, Y. Pan, J. A. Pan, H. J. Song and Z. S. Ma, *RSC Adv.*, 2015, **5**, 68-74.
26. X. Tao, L. Dong, X. Wang, W. Zhang, B. J. Nelson and X. Li, *Adv Mater*, 2010, **22**, 2055-2059.
27. S. Wei, H. Zhang, Y. Huang, W. Wang, Y. Xia and Z. Yu, *Energy & Environmental Science*, 2011, **4**, 736.
28. L. Y. Zhang, Y. Y. Wang, B. Peng, W. T. Yu, H. Y. Wang, T. Wang, B. W. Deng, L. Y. Chai, K. Zhang and J. X. Wang, *Green Chemistry*, 2014, **16**, 3926-3934.
29. X. Gu, C. Lai, F. Liu, W. Yang, Y. Hou and S. Zhang, *J. Mater. Chem. A*, 2015, **3**, 9502-9509.
30. S. H. Chung and A. Manthiram, *Advanced Materials*, 2014, **26**, 1360-1365.
31. , (accessed 2016, 2016).
32. J. Li, F. Qin, L. Zhang, K. Zhang, Q. Li, Y. Lai, Z. Zhang and J. Fang, *Journal of Materials Chemistry A*, 2014, **2**, 13916.
33. M. A. Pimenta, G. Dresselhaus, M. S. Dresselhaus, L. G. Cancado, A. Jorio and R. Saito, *Physical chemistry chemical physics : PCCP*, 2007, **9**, 1276-1291.
34. Z. Xu, D. Cai, Z. Hu, F. Wang and L. Gan, *Electrochimica Acta*, 2014, **117**, 486-491.

35. H. W. Chen, W. L. Dong, J. Ge, C. H. Wang, X. D. Wu, W. Lu and L. W. Chen, *Scientific Reports*, 2013, **3**, 6.
36. X. Wang, X. Fang, X. Guo, Z. Wang and L. Chen, *Electrochimica Acta*, 2013, **97**, 238-243.
37. Y. Wu, M. Gao, X. Li, Y. Liu and H. Pan, *Journal of Alloys & Compounds*, 2014, **608**, 220-228.
38. S. S. Zhang, *Journal of the Electrochemical Society*, 2012, **159**, A920-A923.
39. J. J. Chen, Q. Zhang, Y. N. Shi, L. L. Qin, Y. Cao, M. S. Zheng and Q. F. Dong, *Physical chemistry chemical physics : PCCP*, 2012, **14**, 5376-5382.
40. H. Liu, G. Wang, J. Wang and D. Wexler, *Electrochemistry Communications*, 2008, **10**, 1879-1882.
41. Z. Li, L. Yuan, Z. Yi, Y. Liu, Y. Xin, Z. Zhang and Y. Huang, *Nanoscale*, 2014, **6**, 1653-1660.
42. T. Z. Zhuang, J. Q. Huang, H. J. Peng, L. Y. He, X. B. Cheng, C. M. Chen and Q. Zhang, *Small*, 2016, **12**, 381-389.
43. X. Yang, W. Zhu, G. Cao and X. Zhao, *RSC Adv.*, 2016, **6**, 7159-7171.
44. G. M. Zhou, D. W. Wang, F. Li, P. X. Hou, L. C. Yin, C. Liu, G. Q. Lu, I. R. Gentle and H. M. Cheng, *Energy & Environmental Science*, 2012, **5**, 8901-8906.
45. Q. Qu, T. Gao, H. Zheng, Y. Wang, X. Li, X. Li, J. Chen, Y. Han, J. Shao and H. Zheng, *Advanced Materials Interfaces*, 2015, DOI: 10.1002/admi.201500048, n/a-n/a.
46. S. Liu, K. Xie, Y. Li, Z. Chen, X. Hong, L. Zhou, J. Yuan and C. Zheng, *RSC Adv.*, 2015, **5**, 5516-5522.